Chemical Engineering Journal 500 (2024) 157248

Contents lists available at ScienceDirect

Chemical Engineering Journal

journal homepage: www.elsevier.com/locate/cej

Synergistic chemical traction and pre-intercalation strategies enable high-quality MnO_2 composites for efficient ammonium capture

Shiyong Wang [1], Shuwen Du [1], Yuhao Lei, Lin Zhao, Gang Wang [*]

School of Environment and Civil Engineering, Dongguan University of Technology, Dongguan 523106, Guangdong, PR China

ARTICLE INFO

Keywords:
MnO_2
Chemical traction
Pre-intercalation
Excellent ammonium removal performance
Capacitive deionization

ABSTRACT

The δ-MnO_2 exhibits an ideal capacitive deionization (CDI) electrode for the efficient removal of ammonium ions (NH_4^+), owing to its unique layered structure that facilitates effective insertion and extraction of ions. However, MnO_2 is constrained by self-aggregation, inadequate electrical conductivity, and sluggish reaction kinetics in practical applications, leading to subpar ammonium removal performance. Here, the polyaniline (PANI) intercalated MnO_2 and carbon nanotubes (CNTs) composites (P/M-C-X) were synthesized by a straightforward and swift one-step inorganic/organic interface reaction using the chemical traction effect of aniline. The synergistic effect of the increased layer spacing and the introduced oxygen vacancy after PANI intercalated and the 1D/2D conductive interconnect structure constructed by CNTs can effectively improve the electrical conductivity, promote ions/electrons diffusion, and enhance the charge reaction kinetics. As results, P/M-C-50 exhibits excellent NH_4^+ removal performance, including the maximum salt adsorption capacity (SAC) (160.0 mg g^{-1}), ultra-high salt adsorption rate (SAR) (1.07 mg g^{-1} s^{-1}), and good cyclic stability. Furthermore, the comprehension of NH_4^+ storage mechanism has been enhanced through structural characterization, electrochemical analysis, and theoretical calculation. This study shows that P/M-C-50 has broad potential as a CDI ammonium removal electrode, and lays a solid foundation for the effective recovery and reuse of ammonium resources.

1. Introduction

Human activities have fundamentally altered the nitrogen cycle with excessive use of fertilizers, fine chemicals and increasing nitrogen emissions from livestock, households and industry leading to serious environmental problems such as eutrophication of water bodies, increased greenhouse gas emissions and acidification of water bodies, which have a serious impact on the safety of drinking water sources and fishery products[1–3].The cleanliness of water quality is closely correlated with the ammonium content in water environment. Therefore, the removal of ammonium ions from wastewater and the recovery of ammonium resources not only prevent pollution but also offer cost savings and valuable resource recovery, thus making significant contributions to environmental and resource sustainability[4]. In view of the limitations of environmental capacity and the continuous tightening of ammonia nitrogen emission standards, the existing nitrogen removal processes are facing more stringent technical requirements and challenges. The removal of ammonia nitrogen in wastewater treatment is commonly achieved through conventional biological treatment methods, such as the activated sludge process, which converts it into nitrogen for ammonium removal. However, this method of converting ammonia into elements is contrary to the core concept of the circular economy, which is “reduce, reuse and recycle” [5,6].Other physical and chemical methods, such as ion exchange[7], struvite precipitation[8], and reverse osmosis (RO) [9], have been validated as feasible for removing or recovering NH_4^+ from wastewater. Unfortunately, ion exchange has the disadvantage of potential secondary reactions; struvite precipitation requires the addition of additional chemicals to adjust the pH of the wastewater; and reverse osmosis requires a high-pressure pump as a driving force and is not selective for NH_4^+ during ion removal and does not allow for accurate ammonium recovery. Consequently, there is an urgent necessity to develop a novel technology that can overcome the limitations of existing ammonia recovery methods. This technology should not only address environmental concerns but also facilitate the reuse and recycling of ammonium resources while yielding economic and ecological benefits.

Capacitive deionization (CDI) is a novel desalination technology that has been utilized for treating saline wastewater due to its advantages in

* Corresponding author.
E-mail address: wghy1979@163.com (G. Wang).
[1] Wang and Du equal contribution to this work.

https://doi.org/10.1016/j.cej.2024.157248
Received 26 August 2024; Received in revised form 20 October 2024; Accepted 28 October 2024
Available online 30 October 2024

energy efficiency, ease of operation, environmental sustainability, and cost-effectiveness [10–13]. If CDI technology can be used to treat ammonia wastewater to achieve removal and rapid enrichment and recovery of NH_4^+, and ultimately form a high-value product ammonium fertilizer, the purpose of resource recycling can be achieved, and the dependence on the Haber-Bosch process can also be reduced, thus saving energy and improving economic efficiency. However, the desalination performance of the CDI process heavily relies on the adsorption electrode, which serves as the most crucial component requiring excellent physical and chemical properties. Therefore, developing an efficient electrode material plays a pivotal role in advancing CDI-based ammonium removal technology [14–16]. Traditional carbon-based materials such as graphene [17], carbon aerogel[18,19], and carbon nanotubes [20], which utilize the principle of double electric layer (EDL) to store ions, exhibit insufficient ion capture capacity[21]. Moreover, they inevitably undergo side reactions of carbon anodization, resulting in low desalination capacity [22,23]. In order to overcome these aforementioned shortcomings, research focus has shifted towards Faradaic materials, which boast substantial ion storage capacity due to their reliance on reversible redox reactions or ion insertion effects, and these materials have found successful application as CDI electrodes[24,25].Currently used common Faradaic electrode materials include Prussian blue (PB) and its analogues (PBAs)[26,27], MXene[28,29], transition metal oxides such as manganese oxides(MnO_2)[30,31], NASCION[32], etc. Among them all, MnO_2 stands out due to its low cost, low toxicity, strong acid resistance properties along with a high theoretical capacity (308 mA h g^{-1}) making it suitable for use as an ammonium removal electrode material in CDI[33,34].

Unfortunately, MnO_2 electrode materials have problems such as poor electrical conductivity, insufficient active sites, inadequate structural stability, and slow NH_4^+ reaction kinetics[35]. These problems result in subpar ammonium removal performance, limited cycle life, and low electrochemical reactivity in CDI. To address these challenges, various materials engineering strategies have been developed to enhance the conductivity and redox reaction kinetics of MnO_2 materials by shortening the diffusion path of NH_4^+ ions and increasing the exposed surface area. These strategies include heteroatom doping[36], vacancy formation[37], pre-intercalation[38], and composites with conductive materials[39]. One effective approach is introducing oxygen vacancies to adjust the properties of raw materials by modifying their surface electrical structure. The presence of oxygen vacancies creates additional channels for ion insertion, thereby increasing active site availability and accelerating electron transfer to improve material conductivity[37]. Common methods of introducing oxygen vacancies include heteroatom doping[40], liquid-phase reduction[41], and pre-intercalation[42]. In addition, the inherent self-aggregation properties and poor electrical conductivity of MnO_2 significantly impede the reaction kinetics of NH_4^+. Research have demonstrated that the combination of carbon-based materials with manganese dioxide effectively overcomes this obstacle by facilitating a rapid and efficient electron transfer process, enhancing electron conductivity, and preventing particle agglomeration[39,43]. Besides, pre-intercalation techniques can regulate the interlayer configuration of MnO_2 using common intercalation materials such as polyaniline (PANI)[44] or polyethylpyrrolidone (PVP)[45]. Intercalation not only expands layer spacing but also facilitates NH_4^+ diffusion, thus improving cyclic stability while reducing structural collapse. However, the development and formulation of a straightforward and effective method that can concurrently introduce oxygen vacancies, pre-intercalation, and with conductive materials into MnO_2 to achieve superior NH_4^+ adsorption in CDI remains a significant challenge.

Here, based on the chemical traction effect of aniline and the pre-intercalation strategy, the PANI intercalated MnO_2 and CNTs composites (P/M-C-X) was prepared through a straightforward one-step inorganic/organic interfacial reaction, and then used as a cathode material for CDI to remove NH_4^+.The unique 1D/2D conductive interconnect structure effectively reduces the self-aggregation of MnO_2 nanosheets while providing good electrical conductivity and convenient ion diffusion paths within the composite. Moreover, PANI pre-intercalation not only increases the layer spacing, but also introduces abundant oxygen vacancies, which together provide additional channels for NH_4^+ insertion, thereby improving the current response, increasing the number of redox-active sites, and accelerating electron transfer. Specifically, P/M-C-50 exhibited outstanding ammonium removal properties with significant adsorption/desorption capacity. P/M-C-50 achieved a maximum salt adsorption capacity (SAC) of 160.0 mg g^{-1} and an ultra-high salt adsorption rate (SAR) of 1.07 mg g^{-1} s^{-1}. Furthermore, it demonstrated excellent cyclic stability and holds great promise as a Faradaic electrode material for ammonium removal in CDI.

2. Methods

2.1. Synthesis of P/M-C-50

3 mL aniline monomer and a certain amount of CNTs were dispersed into 150 mL CCl_4 organic solution, and after ultrasound for a period of time, solution A was obtained. 0.4 g of $KMnO_4$ and dissolve it in 150 mL of water to obtain solution b. Add solution b to solution A to create a water/organic stratification system with a distinct interface. After reacting at the water/organic interface for 24 h at 5 ℃, extract and filter the black product, wash it several times with deionized water and ethanol, then freeze-dry it for 24 h to obtain P/M-C-X (X represents the content of CNTs). Specifically, when the amount of added CNTs is determined as 0 mg, 20 mg, 50 mg, or 80 mg, the prepared samples are named P/M-C-0, P/M-C-20, P/M-C-50, or P/M-C-80 respectively. The physical diagram of material preparation is shown in Figure S1.

The details of “Materials characterizations”, “Electrochemical Measurements”, “CDI experiments” and “Density functional theory calculations” are presented in Supplementary materials.

3. Result and discussion

The material preparation process is illustrated in Fig. 1a. The aniline monomer and CNTs were evenly dispersed in the CCl_4 organic solution, while $KMnO_4$ was dissolved in the aqueous phase. At the interface of the two phases, the oxidation reaction of aniline and the reduction reaction of MnO_4^- occurred at the same time, which promoted the layer self-assembly of layered MnO_2 and PANI, and realized the pre-intercalation of PANI (Fig. S1a). It should be noted that the chemical traction effect caused by the electrostatic interaction between CNTs and aniline enables the CNTs were evenly distributed on the surface of MnO_2 nanosheets with intercalated PANI and in the middle of adjacent nanosheets, thus forming a 1D (CNTs)/2D (MnO_2 nanosheets) conductive interconnect structure (Fig. S1b-d). In the absence of aniline monomer, CNTs could not diffuse from the organic phase to the aqueous phase and were still dispersed in the lower organic phase, which further demonstrated the chemical traction effect of aniline (Figure S2). If the solvent was tried to change, the CCl_4 organic phase was replaced with the water phase, although $KMnO_4$ and CNTs could be in direct contact, the experimental results showed (Figure S3) that the product quality after extraction and filtration was not significantly improved. Scanning electron microscopy (SEM) images showed stacked CNTs (Figure S4), clearly indicating that the expected chemical reaction did not occur in the system. Thus, as a contrast, the flower-like pure MnO_2 was prepared by hydrothermal method (Figure S5a), and the specific preparation process has been detailed in Supplementary materials. SEM images of P/M-C-0 and P/M-C-50 are shown in Figure S5b and Fig. 1b. Due to the self-assembly of PANI and MnO_2, the prepared P/M-C-0 showed a typical layered structure. After the introduction of CNTs, CNTs were evenly distributed around MnO_2 nanosheets own to the chemical traction of aniline monomers, forming a unique 1D/2D conductive interconnecting structure, which effectively inhibited the self-aggregation of MnO_2 nanosheets, the free space between adjacent nanosheets is

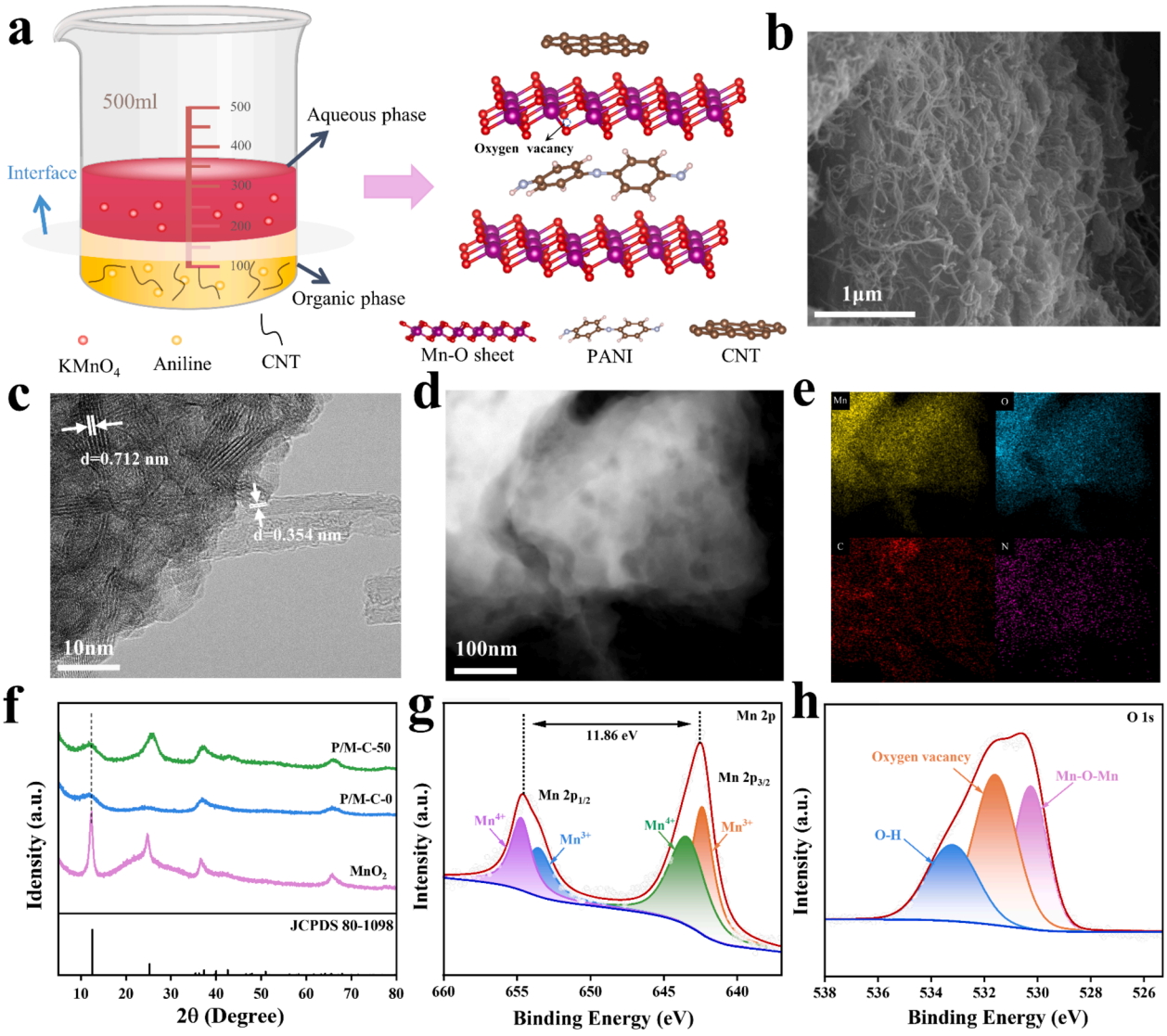

Fig. 1. (a) Schematic synthesis of the P/M-C-50; (b) SEM images of P/M-C-50; (c) HRTEM images of P/M-C-50; (d) HAADF-STEM of P/M-C-50; (e) the corresponding EDS mapping of P/M-C-50; (f) XRD patterns of pristine MnO_2, P/M-C-0, P/M-C-50; (g) Mn 2p, (h) O 1 s of P/M-C-50.

maintained, thus forming a convenient ions/electrons diffusion channel, effectively accelerating ions/electrons migration, and realizing fast ions/electrons diffusion dynamics. The morphologies of P/M-C-20 and P/M-C-80 (Figure S5c and d) were not significantly different from those of P/M-C-50. However, the exterior of P/M-C-20 only covered a limited number of CNTs, while P/M-C-80 showed aggregation of CNTs. The above two morphologies are not conducive to the exposure of active sites and affect the removal performance of ammonium ions. Hence, P/M-C-50 can be considered as the optimal sample. A typical high-resolution transmission electron microscope (HRTEM) image of P/M-C-50 is presented in Fig. 1c, displays two sets of lattice fringes, one of which is about 0.71 nm corresponding to the (0 0 1) crystal plane of MnO_2.The additional set of lattice fringes measures approximately 0.35 nm and corresponds to the (002) crystal plane of the CNTs, providing further evidence of successful integration of the MnO_2 nanosheet with CNTs. The unique 1D/2D conductive interconnect structure formed by the introduction of CNTs facilitates a rational layered structure and prevents the self-aggregation of MnO_2, which improves its structural stability. Additionally, energy dispersive X-ray spectroscopy (EDS) elemental maps reveal a uniform distribution of elements in P/M-C-50 (Fig. 1d-e). HRTEM images of P/M-C-0 (Figure S6a) reveal distinct lattice streaks of typical MnO_2 nanosheets, with a measured interlayer lattice distance of approximately 0.69 nm. Obviously, the lattice stripe size of P/M-C-0 is larger than that of MnO_2 (0.67 nm) (Figure S7), indicating that PANI is successfully intercalated into the interlayer of MnO_2, enlarging the layer spacing and promoting ion diffusion. Compared to P/M-C-0, the layer spacing of P/M-C-50 increases to 0.71 nm, indicating that the introduction of CNTs also contributes to an increased layer spacing for MnO_2, which facilitates ion diffusion and storage.

In order to characterize the prepared samples, various techniques including X-ray diffraction (XRD), X-ray photoelectron spectroscopy (XPS), Raman spectroscopy, FTIR spectroscopy, and other methods were employed to detect their crystal structure, valence state, and vacancy defect state. The XRD pattern (Fig. 1f) demonstrates that the diffraction peaks predominantly occur at approximately 12.03°, 25.85°, 37.17°and 69.94°, corresponding to the (001), (002), (111) and (020) crystal planes of δ-MnO_2 (JCPDS 80–1098), respectively. It is worth noting that in comparison with MnO_2, the XRD patterns of P/M-C-0 and P/M-C-50 reveal a broader and weaker diffraction peak intensity for the (001) crystal phase, accompanied by a shift towards lower angles. This further confirms that the intercalation of PANI leads to an increased layer spacing in MnO_2, which aligns with the HRTEM results. The XRD patterns of other compared samples are presented in Figure S8, showing no

significant deviation from the position of the diffraction peak observed in P/M-C-50. Due to the intercalation of PANI, the XPS spectra of all P/M − C show characteristic peaks of N, Mn and O, which differ from MnO_2 (Figure S9). In the Mn 2P XPS spectrum (Fig. 1g), the peaks observed at 642.44 and 654.3 eV correspond to Mn $2p^{3/2}$ and Mn $2p^{1/2}$, respectively, exhibiting a spin energy difference of 11.86 eV, thereby verifying the characteristic features associated with the MnO_2 phase [46].The four fitting peaks of Mn 2p indicate that Mn^{4+} and Mn^{3+} coexist in MnO_2. Interestingly, the integral area ratio of Mn^{3+}/ Mn^{4+} increases from 0.69 (MnO_2) and 0.78 (P/M-C-0) to 1.21(P/M-C-50) (Figure S10) because the conversion of Mn^{4+} to Mn^{3+} balances the introduced oxygen vacancy. The high-resolution O 1 s spectrum (Fig. 1h) reveals three peaks at 530.24, 531.58, and 533.19 eV, associated with the Mn-O-Mn bond, oxygen vacancy, and O-H bond, respectively [41]. The peak area of oxygen vacancy in P/M-C-50 was significantly higher than that in other samples (Figure S11), indicating that the appropriate introduction of CNTs significantly increased the oxygen vacancy content. In addition, HRTEM images also confirmed the presence of oxygen vacancies in P/M-C-50[47](Figure S12). In the high-resolution N 1 s spectrum of P/M-C-50 (Figure S13c), the peaks at 397.89 and 400.51 eV correspond to the − N = and − N^+− signals, respectively[38], while the peak at 399.53 eV are attributed to the Mn-N bond, as there is a strong interaction between the Mn-N bonds, indicating successful intercalation of MnO_2 by PANI. Additionally, the C1s spectrum (Figure S14c) exhibits five distinct peaks, the presence of C-Mn peak indicates the successful coating of CNTs. The Raman spectra of these five materials exhibit significant characteristic peaks in the 500–700 cm^{-1} range (Figure S15), which can be attributed to the stretching vibration pattern of Mn-O in the [MnO_6] octahedron[45]. Compared with MnO_2, the characteristic peaks of P/M−C samples show a redshift, indicating a decrease in the activation energy of Mn-O bonds, possibly due to the presence of oxygen defects in the [MnO_6] octahedron [36]. Furthermore, the results of FTIR spectroscopy for P/M-C-50 and other compared samples were consistent with those from Raman spectroscopy (Figure S16), further notarizing the aforementioned conclusions. According to Brunauer-Emmett-Teller (BET) tests (Figure S17 and Table S1), it is observed that both P/M-C-0 and P/M-C-50 exhibit substantial specific surface areas of 221.4 m^2/g and 167.5 m^2/g, respectively. Notably, the pore volume of P/M-C-50 (0.27 cm^3 g^{-1}) surpasses that of P/M-C-0 (0.16 cm^3 g^{-1}). P/M-C-50 has a relatively large specific surface area and excellent pore volume, which can strengthen the penetration and transport of ammonium ions, and reveals extra active sites for NH_4^+ adsorption, thus significantly improving the removal performance of ammonium ions.

The electrochemical NH_4^+ storage properties of P/M-C-0, P/M-C-20, P/M-C-50, and P/M-C-80 were assessed through cyclic voltammetry (CV), constant current charge–discharge (GCD), and electrochemical impedance spectroscopy (EIS). The cyclic voltammetry(CV) curves of P/

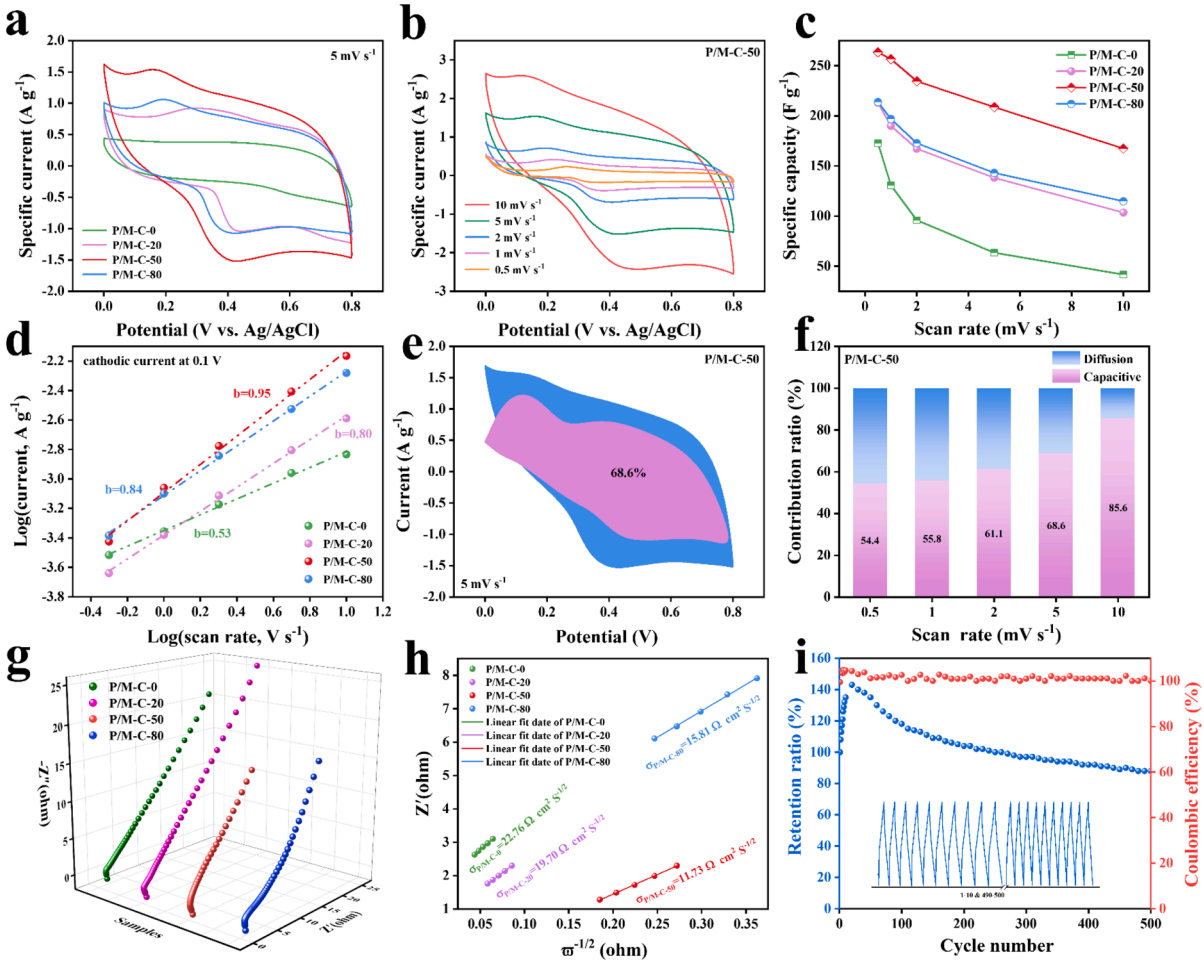

Fig. 2. (a) Cyclic voltammograms of P/M-C-0, P/M-C-20, P/M-C-50, P/M-C-80 at a scan rate of 5 mV/s;(b) CV curves of P/M-C-50 at different sweep rates;(c) Gravimetric specific capacitances of samples at different scan rates;(d) Power-law relationship between particular current and the scanning rate; (e) CV curves showing the capacitive contribution (purple) and diffusion-controlled contributions (blue) for P/M-C-50 at 5 mV s^{-1};(f) Capacitance and diffusion-controlled contributions versus scan rates; (g) EIS spectra; (h) Linear fit showing the corresponding relationship between Z' and $\omega^{-1/2}$ of samples; (i) Cycling performance and coulombic efficiency of P/M-C-50 at 2 A g^{-1}. (For interpretation of the references to colour in this figure legend, the reader is referred to the web version of this article.)

M-C-50 and the reference samples at a scan rate of 5 mV s^{-1} are shown in Fig. 2a and Figure S18. The CV curve of P/M-C-0 was typically rectangular, with no obvious redox peak, while weak redox peaks appeared in P/M-C-20, P/M-C-50 and P/M-C-80, indicating that the introduction of CNTs enhanced the electrical conductivity and promoted the pseudocapacitive characteristics of ion storage [48,49].Among them, P/M-C-50 has the largest area of CV curve, indicating that it has higher ammonium storage capacity and better capacitance performance. This may be attributed to the appropriate introduction of CNTs and the insertion of PANI, which not only form a 1D/2D conductive interconnect structure, but also introduces abundant oxygen vacancies while increasing the MnO_2 layer spacing, enhance the conductivity of the composite material, and promote the rapid transfer and transmission of electrons and ions in the charge and discharge process. The CV curves of P/M-C-50 and other comparison samples were subsequently measured at various scanning rates (Fig. 2b and Figure S19). The CV curves of all samples at high scanning speeds showed no significant distortion, demonstrating excellent rate capability and high reversibility. The specific capacity of different samples at different scanning rates was calculated according to CV curve. With increasing scanning rate, the specific capacity showed a decreasing trend (Fig. 2c). In particular, P/M-C-50 demonstrates the highest specific capacitance at a scanning rate of 0.5 mV s^{-1}, reaching up to 263.4F g^{-1}, indicating its excellent electrochemical performance.

Additionally, the relationship between the current value (i) and the scan rates (v) obeys a power law, expressed as $i = a\nu^b$, where i represents the current value, ν represents the scan rates, and a and b are modifiable parameters. As b is set to 0.5 and 1, the ion storage behavior aligns with diffusion-dominated and capacitive-dominated mechanisms, respectively[50].The b values for P/M-C-0, P/M-C-20, P/M-C-50 and P/M-C-80 are 0.53, 0.80, 0.95 and 0.84, respectively(Fig. 2d), indicating that NH_4^+ storage in P/M-C-50 is driven by both diffusion and capacitive control behaviors with capacitive being dominant. The contribution ratio of diffusion to capacitive can be precisely quantified by the following calculation formula ($i = k_1\nu + k_2\nu^{1/2}$, where $k_1\nu$ represents the capacitive contribution and $k_2\nu^{1/2}$ represents the ion diffusion contribution[35,51]). The capacitive contribution of P/M-C-50 reaches 68.6 % at a scan rate of 5 mV s^{-1} (Fig. 2e), significantly higher than that of P/M-C-0(17.9 %), P/M-C-20(54.4 %) and P/M-C-80 (61.1 %) (Figure S20a-c). The capacitive contribution is positively correlated with scan rate (Fig. 2f) and the maximum capacitive contribution of the P/M-C-50 reaches 85.6 % at a scan rate of 10 mV s^{-1}. Obviously, P/M-C-50 with high capacitive contribution can exhibit a more efficient electron transfer process, ensuring the effective and swift removal of NH_4^+ in the CDI process. [51]. Besides, the large layer spacing, abundant oxygen vacancies and 1D/2D interconnect network structure of P/M-C-50, not only contribute to the enhancement capacitive contribution, but also improve the charge transfer and ion diffusion during charge and discharge, thus promoting the rapid reversible insertion/extraction of NH_4^+.

EIS was utilized for further investigation into the factors contributing to the improved storage performance of NH_4^+ (Fig. 2g). All electrodes exhibited a semicircular response in the high frequency region and a linear response in the low frequency region. The small diameter of the semicircle for all electrodes indicates low resistance and fast charge transfer, attributed to the introduction of oxygen vacancies and CNT. Moreover, by plotting the correlation coefficient between Z' and $\omega^{-1/2}$ (where ω is angular frequency), the Warburg coefficient can be determined [52]. As shown in Fig. 2h, P/M-C-50 electrode has the smallest slope, indicating a faster diffusion rate for NH_4^+ ions. By calculation, it is found that the diffusion coefficient of P/M-C-50 is 1.6×10^{-17} cm^2 s^{-1} is significantly larger than that of P/M-C-0 (4.3×10^{-18} cm^2 s^{-1}), P/M-C-20 (5.7×10^{-18} cm^2 s^{-1}), and P/M-C-80 (8.8×10^{-18} cm^2 s^{-1}), indicating that it has the best ion diffusion performance and is conducive to the rapid removal of ammonium ions. The GCD curves of all samples are depicted in Figure S21, showing that P/M-C-50 exhibits the highest specific capacity at various scanning rates, consistent with the CV results. The GCD curve of P/M-C-50 reveals a charging buffer platform between 0.2 and 0.4 V at a low current density (1 A g^{-1}), indicating capacitive behavior. Furthermore, both P/M-C-0 and P/M-C-50 demonstrate longer cycle stability compared to MnO_2. At a current density of 2 A/g (Fig. 2i), P/M-C-50 retains 88 % of its capacity after 500 cycles, surpassing both MnO_2 (32 %) and P/M-C-0 (86 %) (Figure S22), highlighting the significantly enhanced structural stability of P/M-C-50. Therefore, P/M-C-50 demonstrates excellent electrochemical ammonium storage performance and shows great potential as an electrode material for CDI ammonium ions removal. This not only offers an effective strategy for recovering ammonium resources from actual wastewater, but also provides important theoretical support and practical reference for the reuse and recycling of ammonium resources.

To evaluate the ammonium ions removal performance of the prepared material, a CDI module was constructed with activated carbon (AC) as the anodic material for Cl^- capture and MnO_2-based material as the cathode for NH_4^+ capture (Fig. 3a). At lower ammonium ion concentrations (0–400 mg L^{-1}), the NH_4Cl concentration is linearly correlated with the conductivity (Figure S23). The impact of different voltages on SAC was initially examined in an NH_4^+ solution with an initial concentration of 100 mg L^{-1} (Figure S24). As voltage increases from 0.8 V to 1.4 V, the SAC of P/M-C-50 gradually rises, reaching its peak at 1.4 V due to the heightened electrostatic driving force, the electrode's ion intercalation capacity is markedly improved. The ions removal performance of all prepared samples was compared and analyzed at different NH_4^+ concentrations (Fig. 3b). SAC showed a significant increase with the rise in NH_4^+ solution concentration. Notably, P/M-C-50 exhibited the highest SAC value at each concentration compared to the other three samples. This excellent ions removal performance can be attributed to the conductive bridge constructed by the CNTs and the enhanced layer spacing after PANI intercalated, which promotes charge transfer and provides a wide diffusion and short path for NH_4^+ diffusion. Additionally, the presence of oxygen vacancy provides more active sites for the rapid reversible intercalation/deintercalation of NH_4^+, thus greatly enhancing the salt adsorption capacity of the composite. All these results prove the success of chemical traction effect and pre-intercalation strategy.

In Fig. 3c, P/M-C-50 reached adsorption equilibrium fastest in NH_4^+ solutions with an initial concentration of 100 mg L^{-1}, and SAC value was the highest (123.4 mg g^{-1}), which was 2.11 times that of MnO_2 (Figure S25), 2.01 times that of P/M-C-0, and 1.26 times that of P/M-C-20 and 1.21 times that of P/M-C-80, respectively. In addition, SAR and SAC of Ragone diagram (Fig. 3d) can intuitively reflect ion removal performance. Obviously, the P/M-C-50 curve was in the upper right position, which means that the largest SAC and the fastest SAR (0.59 mg g^{-1} s^{-1}). It is fully demonstrated that P/M-C-50 has excellent ion trapping performance and rapid ion removal efficiency in NH_4^+ solution treatment. In the practical application of CDI technology, it is crucial to achieve efficient ammonium ions removal performance within a specific concentration range due to the significant difference in ammonium-containing wastewater. To further investigate the ammonium removal properties of P/M-C-50, NH_4^+ solutions ranging from 25 to 400 mg L^{-1} were tested at a voltage of 1.4 V (Fig. 3e). The results indicated that SAC increased with the rise in NH_4^+ concentration. Particularly, in a 400 mg L^{-1} NH_4^+ solution, the SAC of P/M-C-50 reached as high as 160.0 mg g^{-1}, which significantly outperforms P/M-C-0 (106.2 mg g^{-1}), P/M-C-20 (131.7 mg g^{-1}), and P/M-C-80 (141.9 mg g^{-1}). Clearly, the Ragone diagram for NH_4^+ at 400 mg L^{-1} (Fig. 3f) is positioned at the top right corner, fully demonstrating the exceptional ion trapping capability of P/M-C-50 even under high brine concentrations. Compared with the recently published literature, our prepared P/M-C-50 also has greater advantages in ammonium ion removal performance (Table S2 and Fig. 3g). The P/M-C-50 demonstrates lower specific energy consumption (SEC) and superior charging efficiency at any NH_4^+ concentration in comparative studies, attributed to its exceptional salt adsorption

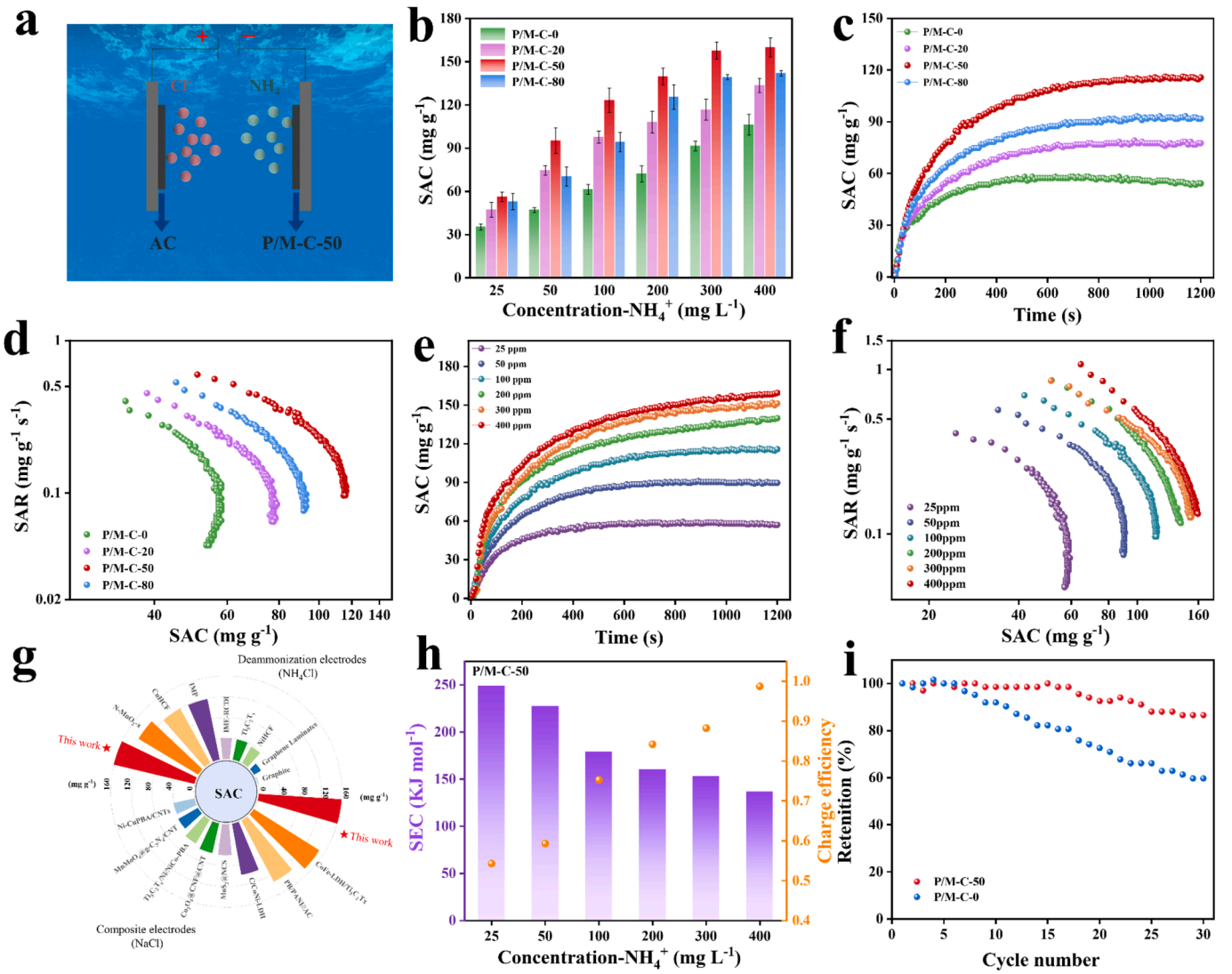

Fig. 3. (a) Schematic diagram of CDI cell;(b) SAC of samples at various voltages; (c) SAC and (d) Ragone plot of samples in 100 mg L^{-1} NH_4^+ solution using an applied voltage of 1.4 V; (e) SAC and (f) Ragone plot of P/M-C-50 in various NH_4^+ solution using an applied voltage of 1.4 V; (g) Comparison of deammonization performances of the P/M-C-50 and those based on other reported electrode materials; (h) The specific energy consumption and charge efficiency of P/M-C-50 in various NH_4^+ concentrations; (i) Recycling performance.

capacity (SAC) and rapid salt removal rate. Even at a voltage of 1.4 V, the P/M-C-50 can still maintain a charge efficiency of 0.98 and an SEC value of 136.8 kJ/mol (Fig. 3h), outperforming P/M-C-0, P/M-C-20, and P/M-C-80 (Figure S26). Furthermore, the cyclic stability of the P/M-C-50 electrode was investigated through conducting 30 consecutive adsorption–desorption experiments. The results, as depicted in Fig. 3i, demonstrate that the SAC retention rate of P/M-C-50 can reach 86.6 %, which is significantly higher than that of P/M-C-0 (59.6 %), indicating excellent stably performance. This outstanding recycling performance can be attributed to the abundant oxygen vacancy, which enhances electron transfer rate and improves electrical conductivity of the composite material, facilitating rapid electron transfer during adsorption–desorption processes. Additionally, the introduction of CNTs not only further improves the conductivity of the composite, but also enhances its stability.

The basic mechanism of NH_4^+ removal by the P/M-C-50 electrode during the CDI process was investigated through a series of characterization tests, including ex situ XRD and XPS analysis, to monitor the structural evolution and chemical state changes of the electrode. The XPS Mn 2p spectra of P/M-C-50 electrodes in NH_4^+ intercalation/deintercalation process under different states are illustrated in Fig. 4a-c. Compared with the original state of P/M-C-50 (Fig. 1g), the integral area ratio of Mn^{3+}/Mn^{4+} after the first ammonium ion intercalation process increases from 1.21 to 1.66, which clearly indicates that the insertion of NH_4^+ ions is closely related to the conversion process of Mn^{4+} to Mn^{3+}. After the first NH_4^+ deintercalation, the integral area ratio of Mn^{3+}/Mn^{4+} fell to 1.16, which was similar to the original sample, which fully verified the reversibility of the redox reaction between Mn^{3+} and Mn^{4+}. To ensure the reliability of the above observations, we further tested the samples from the second and third cycles. After NH_4^+ intercalation in the second cycle, the integral area ratio of Mn^{3+}/Mn^{4+} increases to 1.76, and decreases to 1.20 after removal. After the third cycle, after NH_4^+ intercalation and deintercalation, the integral area ratio of Mn^{3+}/Mn^{4+} is 1.69 and 1.20, respectively. The results of the three cycles are highly consistent, which not only confirms the reversibility of NH_4^+ intercalation, but also demonstrates the stability of NH_4^+ intercalation/deintercalation during CDI.

The XRD pattern of P/M-C-50 after the NH_4^+ ion insertion and extraction process is presented in Figure S27. Following NH_4^+ intercalation, the characteristic peak of the (001) crystal surface shifts to a lower angle compared to the original P/M-C-50, indicating an expansion of the crystal lattice. Upon removal of NH_4^+, the characteristic peak

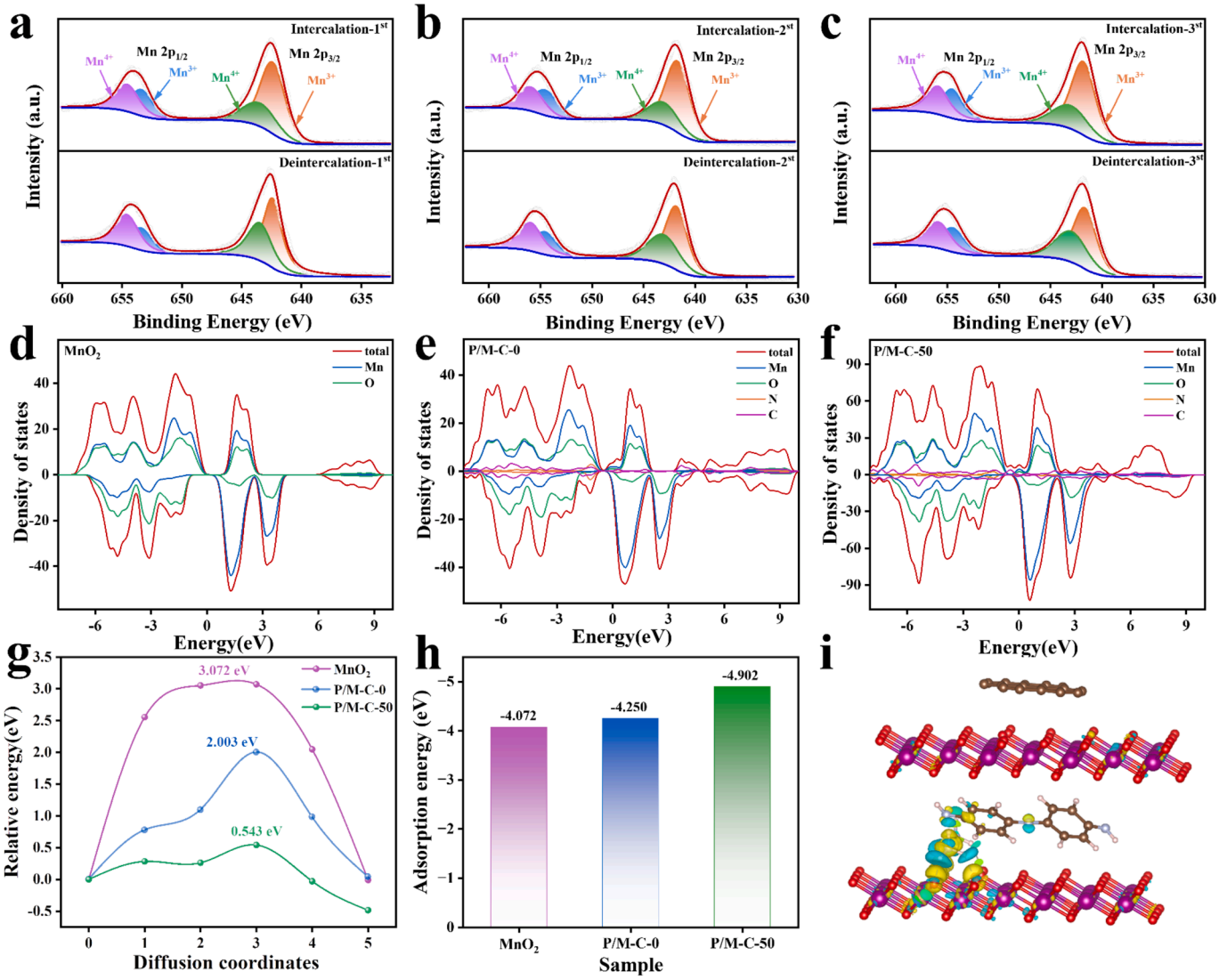

Fig. 4. (a-c) XPS Mn 2p spectra; (d-f) The DOS of MnO_2, P/M-C-0 and P/M-C-50; (g) diffusion barriers profiles, (h)adsorption energy of NH_4^+ for MnO_2, P/M-C-0 and P/M-C-50; (i) Charge density differences of NH_4^+ adsorption in the interlayer of P/M-C-50. The yellow and cyan electron clouds show accumulation and depletion of electrons, respectively. The isosurface value is 0.002 e $Bohr^{-3}$. (For interpretation of the references to colour in this figure legend, the reader is referred to the web version of this article.)

returns to its initial position, suggesting a contraction process in the lattice, corresponding to the contraction and expansion during NH_4^+ adsorption/desorption. Notably, the lattice parameter decreases from 12.18 to 11.86 after NH_4^+ intercalation and increases to 12.21 after deintercalation. This small lattice parameter change during the CDI process not only demonstrates the excellent structural reversible stability of P/M-C-50, but also predicts its excellent regeneration performance, thus maintaining a high SAC retention rate in 30 consecutive adsorption–desorption experiments. Additionally, N 1 s XPS spectrum exhibits a shift towards increased binding energy upon NH_4^+ intercalation (Figure S28), further revealing interaction between NH_4^+ and P/M-C-50.

The action mechanism of P/M-C-50 in the process of CDI NH_4^+ removal was further understood through calculation based on density function theory (DFT). The electron state density (DOS) of MnO_2, P/M-C-0, and P/M-C-50 is depicted in Fig. 4d-f, with the structure model shown in Figure S29. In comparison to MnO_2, the DOS of P/M-C-0 shifts towards lower energy, causing the Fermi level to enter the conduction band and facilitating an easier transition of electrons from the valence band to the conduction band. This results in an increased number of free electrons in the conduction band and significantly enhances the conductivity of P/M-C-0 after introducing PANI. As for P/M-C-50, higher DOS intensity near the Fermi level indicates greater participation of free electrons in conductive processes after introducing CNTs, leading to improved conductivity. It is evident that the conductivity of P/M-C-50 is significantly enhanced, effectively promoting electron and ion transport dynamics during CDI ammonium removal. Furthermore, according to the migration model (Figure S30), the NH_4^+ ion diffusion barrier calculated for P/M-C-0, rich in oxygen vacancies, is 2.003 eV, which is smaller than that for MnO_2 without oxygen vacancies (3.072 eV) (Fig. 4g). This suggests that oxygen vacancies can enhance NH_4^+ ion diffusion. P/M-C-50 exhibits an even lower diffusion barrier (0.543 eV), indicating that the introduction of CNTs further reduces the barrier for NH_4^+ ion diffusion and facilitates rapid migration of NH_4^+ ion. Therefore, optimizing the material structure can significantly improve ion transport performance and enhance ammonium ions removal efficiency. The adsorption structure model of NH_4^+ (Figure S31) demonstrates that NH_4^+ can achieve stable adsorption on MnO_2, P/M-C-0, and P/M-C-50. P/M-C-0 with abundant oxygen vacancies has a lower adsorption energy (−4.250 eV) than MnO_2 (Fig. 4h), indicating that oxygen vacancy is favorable for NH_4^+ adsorption Otherwise, P/M-C-50, which has the highest oxygen vacancy content, has the lowest adsorption energy

(−4.902 eV), indicating the strongest binding strength and more favorable adsorption of NH_4^+.Then, the charge density distribution of MnO_2 (Figure S32a), P/M-C-0 (Figure S32b), and P/M-C-50 (Fig. 4i) after NH_4^+ intercalating was analyzed. The charge transfers between NH_4^+ and P/M-C-50 is 0.79 e^-, much lower than the charge transfer between NH_4^+ and MnO_2(1.79 e^-), P/M-C-0 (1.46 e^-). The reduction in charge transfer indicates that the electronic interaction between NH_4^+ and the P/M-C-50 is reduced, which may be due to the introduction of PANI and CNTs that changed the surface properties and electronic structure of MnO_2, providing more adsorption sites, making it easier for to adsorb on P/M-C-50. Additionally, the weaker electrostatic interaction between NH_4^+ and P/M-C-50 further facilitated the diffusion of NH_4^+.

4. Conclusion

In conclusion, the PANI intercalated MnO_2 and CNTs composites were prepared by chemical traction effect and pre-intercalation strategy. The increased layer spacing and oxygen vacancy introduced after PANI intercalated and the 1D/2D conductive interconnect structure constructed by CNT together improve the ammonium ion removal performance of CDI system. As a result of these advantages, P/M-C-50 electrode demonstrated high SAC (160.0 mg g^{-1}), lower energy consumption (136.8 kJ/mol), and good cycling performance (SAC retention of 86.6 % is maintained following 30 cycles), when serving as a CDI electrode to remove NH_4^+ ions. Notably, the ammonium ions removal performance of P/M-C-50 surpassed that of most reported electrode materials. Furthermore, through spectroscopy studies and theoretical calculations, a deeper understanding of the mechanism of NH_4^+ removal and the structural stability of composite materials was achieved. This work presents a simple and efficient method to construct 1D/2D conductive interconnect structures with high interconnectivity and integrity. This successful material combination not only provides valuable inspiration for future designs of other 1D materials composited with 2D materials, but also heralds the great potential of materials with this structure as a high-performance Faradaic CDI ammonium ion removal electrode, which promises to achieve even better performance.

CRediT authorship contribution statement

Shiyong Wang: Writing – review & editing, Writing – original draft, Resources, Methodology, Formal analysis. **Shuwen Du:** Writing – review & editing, Writing – original draft, Formal analysis, Data curation. **Yuhao Lei:** Methodology, Formal analysis. **Lin Zhao:** Formal analysis. **Gang Wang:** Supervision, Resources.

Declaration of competing interest

The authors declare that they have no known competing financial interests or personal relationships that could have appeared to influence the work reported in this paper.

Acknowledgments

The authors acknowledge financial support from the National Natural Science Foundation of China (22108032 and 22178055), Dongguan Introduction Program of Leading Innovative and Entrepreneurial Talents, and the support of characterization from Dongguan University of Technology Analytical and Testing Center.

Appendix A. Supplementary data

Supplementary data to this article can be found online at https://doi.org/10.1016/j.cej.2024.157248.

Data availability

No data was used for the research described in the article.

References

[1] C. Yu, X. Huang, H. Chen, H.C.J. Godfray, J.S. Wright, J.W. Hall, P. Gong, S. Ni, S. Qiao, G. Huang, Y. Xiao, J. Zhang, Z. Feng, X. Ju, P. Ciais, N.C. Stenseth, D. O. Hessen, Z. Sun, L. Yu, W. Cai, H. Fu, X. Huang, C. Zhang, H. Liu, J. Taylor, Managing nitrogen to restore water quality in China, Nature 567 (7749) (2019) 516–520, https://doi.org/10.1038/s41586-019-1001-1.
[2] N. Gruber, J.N. Galloway, An Earth-system perspective of the global nitrogen cycle, Nature 451 (7176) (2008) 293–296, https://doi.org/10.1038/nature06592.
[3] D.E. Canfield, A.N. Glazer, P.G. Falkowski, The evolution and future of Earth's nitrogen cycle, Science 330 (6001) (2010) 192–196, https://doi.org/10.1126/science.1186120.
[4] M. Rodrigues, R.J. Lund, A. ter Heijne, T. Sleutels, C.J.N. Buisman, P. Kuntke, Application of ammonium fertilizers recovered by an Electrochemical System, Resour. Conserv. Recycl. 181 (2022) 106225, https://doi.org/10.1016/j.resconrec.2022.106225.
[5] Y. Sun, Y. Guan, M. Pan, X. Zhan, Z. Hu, G. Wu, Enhanced biological nitrogen removal and N_2O emission characteristics of the intermittent aeration activated sludge process, Rev. Environ. Sci. Bio/Technol. 16 (4) (2017) 761–780, https://doi.org/10.1007/s11157-017-9444-z.
[6] V. Prieto-Sandoval, C. Jaca, M. Ormazabal, Towards a consensus on the circular economy, J. Clean. Prod. 179 (2018) 605–615, https://doi.org/10.1016/j.jclepro.2017.12.224.
[7] S. Tabassum, A combined treatment method of novel Mass Bio System and ion exchange for the removal of ammonia nitrogen from micro-polluted water bodies, Chem. Eng. J. 378 (2019) 122217, https://doi.org/10.1016/j.cej.2019.122217.
[8] L. Hu, J. Yu, H. Luo, H. Wang, P. Xu, Y. Zhang, Simultaneous recovery of ammonium, potassium and magnesium from produced water by struvite precipitation, Chem. Eng. J. 382 (2020) 123001, https://doi.org/10.1016/j.cej.2019.123001.
[9] D.L. McCurry, K.P. Ishida, G.L. Oelker, W.A. Mitch, Reverse osmosis shifts chloramine speciation causing re-formation of NDMA during potable reuse of wastewater, Environ. Sci. Tech. 51 (15) (2017) 8589–8596, https://doi.org/10.1021/acs.est.7b01641.
[10] M. Liang, N. Liu, X. Zhang, Y. Xiao, J. Yang, F. Yu, J. Ma, A reverse-defect-engineering strategy toward high edge-nitrogen-doped nanotube-like carbon for high-capacity and stable sodium ion capture, Adv. Funct. Mater. 32 (49) (2022) 2209741, https://doi.org/10.1002/adfm.202209741.
[11] L. Guo, J. Zhang, M. Ding, C. Gu, S. Vafakhah, W. Zhang, D.-S. Li, P. Valdiviay Alvarado, H.Y. Yang, Hierarchical Co_3O_4/CNT decorated electrospun hollow nanofiber for efficient hybrid capacitive deionization, Sep. Purif. Technol. 266 (2021) 118593, https://doi.org/10.1016/j.seppur.2021.118593.
[12] S. Gong, H. Liu, F. Zhao, Y. Zhang, H. Xu, M. Li, J. Qi, H. Wang, C. Li, W. Peng, X. Fan, J. Liu, Vertically aligned bismuthene nanosheets on MXene for High-performance capacitive deionization, ACS Nano 17 (5) (2023) 4843–4853, https://doi.org/10.1021/acsnano.2c11430.
[13] X. Tu, Y. Liu, K. Wang, Z. Ding, X. Xu, T. Lu, L. Pan, Ternary-metal Prussian blue analogues as high-quality sodium ion capturing electrodes for rocking-chair capacitive deionization, J. Colloid Interface Sci. 642 (2023) 680–690, https://doi.org/10.1016/j.jcis.2023.04.007.
[14] X. Liu, X. Xu, X. Xuan, W. Xia, G. Feng, S. Zhang, Z.-G. Wu, B. Zhong, X. Guo, K. Xie, Y. Yamauchi, Unlocking enhanced capacitive deionization of $NaTi_2(PO_4)_3$/carbon materials by the yolk-shell design, J. Am. Chem. Soc. 145 (16) (2023) 9242–9253, https://doi.org/10.1021/jacs.3c01755.
[15] J. Ma, L. Chen, F. Yu, Environmental applications and perspectives of flow electrode capacitive deionization (FCDI), Sep. Purif. Technol. 335 (2024) 126095, https://doi.org/10.1016/j.seppur.2023.126095.
[16] S. Wang, G. Wang, C. He, N. Gao, B. Lu, L. Zhao, J. Weng, S. Zeng, C. Li, Enabling superior hybrid capacitive deionization performance in NASICON-structured $Na_3MnTi(PO_4)_3$/C by incorporating a two-species redox reaction, J. Mater. Chem. A 9 (11) (2021) 6898–6904, https://doi.org/10.1039/d0ta11042f.
[17] P. Liu, T. Yan, L. Shi, H.S. Park, X. Chen, Z. Zhao, D. Zhang, Graphene-based materials for capacitive deionization, J. Mater. Chem. A 5 (27) (2017) 13907–13943, https://doi.org/10.1039/c7ta02653f.
[18] C. Macías, G. Rasines, P. Lavela, M.C. Zafra, J.L. Tirado, C.O. Ania, Mn-containing N-doped monolithic carbon aerogels with enhanced macroporosity as electrodes for capacitive deionization, ACS Sustain. Chem. Eng. 4 (5) (2016) 2487–2494, https://doi.org/10.1021/acssuschemeng.5b01444.
[19] W. Luo, C. Shi, S. Wang, H. Liu, Y. Zhang, Y. Song, J. Zhao, L. Zhang, Z. Ling, Carbon coated vermiculite aerogels by quick pyrolysis as cost-effective and scalable solar evaporators, Desalination 566 (2023) 116886, https://doi.org/10.1016/j.desal.2023.116886.
[20] Y. Wimalasiri, L. Zou, Carbon nanotube/graphene composite for enhanced capacitive deionization performance, Carbon 59 (2013) 464–471, https://doi.org/10.1016/j.carbon.2013.03.040.
[21] S.-W. Tsai, D.V. Cuong, C.-H. Hou, Selective capture of ammonium ions from municipal wastewater treatment plant effluent with a nickel hexacyanoferrate electrode, Water Res. 221 (2022) 1187867, https://doi.org/10.1016/j.watres.2022.118786.

[22] X. Liu, D. Rehman, Y. Shu, B. Liu, L. Wang, L. Li, M. Wang, K. Wang, Q. Han, L. Zang, J.H. Lienhard, Z. Wang, Selective fluoride removal from groundwater using CNT-CeO_2 electrodes in capacitive deionization (CDI), Chem. Eng. J. 482 (2024) 149097, https://doi.org/10.1016/j.cej.2024.149097.

[23] S. Wang, H. Zhuang, X. Shen, L. Zhao, Z. Pan, L. Liu, S. Lv, G. Wang, Copper removal and recovery from electroplating effluent with wide pH ranges through hybrid capacitive deionization using CuSe electrode, J. Hazard. Mater. 457 (2023) 131785, https://doi.org/10.1016/j.jhazmat.2023.131785.

[24] J. Ma, R. Zhou, F. Yu, Hotspots and future trends of capacitive deionization technology: A bibliometric review, Desalination 571 (2024) 117107, https://doi.org/10.1016/j.desal.2023.117107.

[25] L. Zhang, Y. Wang, Y. Cai, R. Fang, S. Huang, Y. Zhao, S. Zhang, Heterostructure of NiCoAl-layered double hydroxide nanosheet arrays assembled on MXene coupled with CNT as conductive bridge for enhanced capacitive deionization, Chem. Eng. J. 478 (2023) 147270, https://doi.org/10.1016/j.cej.2023.147270.

[26] S. Wang, Z. Pan, Z. Li, H. Zhuang, L. Zhao, Z. Li, Y. Lei, G. Wang, CNT/copper hexacyanoferrate: A superior Faradic electrode for ammonium ion removal with stable performance and high capacity, Chem. Eng. J. 466 (2023) 143163, https://doi.org/10.1016/j.cej.2023.143163.

[27] Q. Wang, Q. Wu, M. Zhao, S. Lu, D. Liang, Prussian blue analogue based integrated membrane electrodes for desalination and selective removal of ammonium ions in a rocking-chair capacitive deionization, Chem. Eng. J. 482 (2024) 148923, https://doi.org/10.1016/j.cej.2024.148923.

[28] J. Lei, F. Yu, H. Xie, J. Ma, Ti_3C_2TxMXene/carbon nanofiber multifunctional electrode for electrode ionization with antifouling activity, Chem. Sci. 14 (13) (2023) 3610–3621, https://doi.org/10.1039/d2sc06946f.

[29] Y. Zhang, S. Wang, D. Han, H. Chen, H. Liu, J. Zhu, W. Luo, C. Shi, Y. Song, Z. Ling, 3D macroporous MXene/sodium alginate aerogels with “brick-concrete” structures for highly efficient solar-driven water purification, Desalination 585 (2024) 117772, https://doi.org/10.1016/j.desal.2024.117772.

[30] Y.-H. Tu, H.-Y. Huang, Y.-H. Yang, C.-Y. Lai, C.-W. Tai, C.-C. Hu, Comprehensive Study on the Ion-Selective Behavior of MnOx for Electrochemical Deionization, ACS Appl. Mater. Interfaces 15 (40) (2023) 46812–46828, https://doi.org/10.1021/acsami.3c08271.

[31] Y. Li, Y. Wang, Y. Cai, R. Fang, L. Zhang, The exploration and comparison of adsorption mechanisms in MnO_2 with different crystal structures for capacitive deionization, Desalination 577 (2024) 117387, https://doi.org/10.1016/j.desal.2024.117387.

[32] O. Sufiani, H. Tanaka, K. Teshima, R.L. Machunda, Y.A.C. Jande, Research progress of sodium super ionic conductor electrode materials for capacitive deionization, Sep. Purif. Technol. 340 (2024) 126830, https://doi.org/10.1016/j.seppur.2024.126830.

[33] F. Wang, Y. Zheng, Q. Chen, Z. Yan, D. Lan, E. Lester, T. Wu, A critical review of facets and defects in different MnO_2 crystalline phases and controlled synthesis – Its properties and applications in the energy field, Coord. Chem. Rev. 500 (2024) 215537, https://doi.org/10.1016/j.ccr.2023.215537.

[34] X. Gao, Z. Fu, Y. Sun, D. Wang, X. Wang, Z. Hou, J. Wang, X. Liu, S. Wang, S. Yao, H. Zhang, S. Li, Z. Tang, W. Fu, K. Nie, J. Xie, Z. Yang, Y.-M. Yan, Efficient hybrid capacitive deionization with MnO_2/g-C_3N_4 heterostructure: Enhancing Mn dz_2 electron occupancy by interfacial electron bridge for fast charge transfer, Desalination 567 (2023) 116981, https://doi.org/10.1016/j.desal.2023.116981.

[35] Y. Chen, S. Pu, Z. Zhang, M. Gao, W. Deng, F. Chen, W. Chen, T. Ao, Y. Zhang, The ions storage mechanism of capacitive-faradic coupling effect for pseudo-intercalation electrode MnO_2, Sep. Purif. Technol. 330 (2024) 125529, https://doi.org/10.1016/j.seppur.2023.125529.

[36] X. Cai, Y. Liu, J. Zha, F. Tan, B. Zhang, W. Yan, J. Zhao, B. Lu, J. Zhou, C. Tan, A flexible and safe planar zinc-ion micro-battery with ultrahigh energy density enabled by interfacial engineering for wearable sensing systems, Adv. Funct. Mater. 33 (29) (2023) 2303009, https://doi.org/10.1002/adfm.202303009.

[37] S. Wang, L. Zhao, Y. Lei, Z. Li, G. Wang, N-doped MnO_2 with abundant oxygen vacancies achieves high-capacity and stable ammonium ion capture by capacitive deionization, Sep. Purif. Technol. 329 (2024) 125204, https://doi.org/10.1016/j.seppur.2023.125204.

[38] C. Zuo, F. Chao, M. Li, Y. Dai, J. Wang, F. Xiong, Y. Jiang, Q. An, Improving Ca-ion storage dynamic and stability by interlayer engineering and Mn-dissolution limitation based on robust MnO_2@PANI hybrid cathode, Adv. Energy Mater. 13 (30) (2023) 2301014, https://doi.org/10.1002/aenm.202301014.

[39] W. Shi, X. Zhou, J. Li, E.R. Meshot, A.D. Taylor, S. Hu, J.-H. Kim, M. Elimelech, D. L. Plata, High-performance capacitive deionization via manganese oxide-coated, vertically aligned carbon nanotubes, Environ. Sci. Technol. Lett. 5 (11) (2018) 692–700, https://doi.org/10.1021/acs.estlett.8b00397.

[40] T. Yao, H. Wang, X. Ji, D. Wang, Q. Zhang, L. Meng, J.W. Shi, X. Han, Y. Cheng, Introducing hybrid defects of silicon doping and oxygen vacancies into MOF-Derived $TiO_{(2-X)}$ @carbon nanotablets toward high-performance sodium-ion storage, Small 19 (38) (2023) 2302831, https://doi.org/10.1002/smll.202302831.

[41] Y. Wang, Y. Zhang, G. Gao, Y. Fan, R. Wang, J. Feng, L. Yang, A. Meng, J. Zhao, Z. Li, Effectively modulating oxygen vacancies in flower-like delta-$MnO_{(2)}$ nanostructures for large capacity and high-rate zinc-ion storage, Nanomicro Lett 15 (1) (2023) 219, https://doi.org/10.1007/s40820-023-01194-3.

[42] W. Lv, J. Meng, Y. Li, W. Yang, Y. Tian, X. Lyu, C. Duan, X. Ma, Y. Wu, Inexpensive and eco-friendly nanostructured birnessite-type δ-MnO_2: A design strategy from oxygen defect engineering and K^+ pre-intercalation, Nano Energy 98 (2022) 107274, https://doi.org/10.1016/j.nanoen.2022.107274.

[43] Y. Liu, C. Xie, X. Li, Carbon nanotube network induces porous deposited $MnO_{(2)}$ for high-areal capacity Zn/Mn batteries, 2402026, Small (2024), https://doi.org/10.1002/smll.202402026.

[44] J. Huang, Z. Wang, M. Hou, X. Dong, Y. Liu, Y. Wang, Y. Xia, Polyaniline-intercalated manganese dioxide nanolayers as a high-performance cathode material for an aqueous zinc-ion battery, Nat. Commun. 9 (1) (2018) 2906, https://doi.org/10.1038/s41467-018-04949-4.

[45] A. Zhang, R. Zhao, Y. Wang, J. Yue, J. Yang, X. Wang, C. Wu, Y. Bai, Hybrid superlattice-triggered selective proton Grotthuss intercalation in δ-MnO_2 for high-performance zinc-ion battery, 2313163, Angew. Chem. Int. Ed. (2023), https://doi.org/10.1002/anie.202313163.

[46] H. Wang, R. Guo, Y. Ma, F. Zhou, Cross-doped Mn/Mo oxides with core-shell structures designed by a self-template strategy for durable aqueous zinc-ion batteries, Adv. Funct. Mater. 33 (38) (2023) 2301351, https://doi.org/10.1002/adfm.202301351.

[47] G. Cui, Y. Zeng, J. Wu, Y. Guo, X. Gu, X.W.D. Lou, Synthesis of nitrogen-doped K $Mn_{(8)}$ $O_{(16)}$ with oxygen vacancy for stable zinc-ion batteries, Adv. Sci. (Weinh) 9 (10) (2022) 2106067, https://doi.org/10.1002/advs.202106067.

[48] Q. Chen, J. Jin, M. Song, X. Zhang, H. Li, J. Zhang, G. Hou, Y. Tang, L. Mai, L. Zhou, High-energy aqueous ammonium-ion hybrid supercapacitors, Adv. Mater. 34 (8) (2022) 2107992, https://doi.org/10.1002/adma.202107992.

[49] Y. Liu, B. Geng, Y. Zhang, X. Gao, X. Du, X. Dou, H. Zhu, X. Yuan, MnO_2 decorated porous carbon derived from Enteromorpha prolifera as flow-through electrode for dual-mode capacitive deionization, Desalination 504 (2021) 114977, https://doi.org/10.1016/j.desal.2021.114977.

[50] Z. Liu, B. Wei, K. Liu, L. Wang, DBS^--doped polypyrrole/CNTs with 3D conductive architecture connected with MoS_2 as symmetrical electrodes for boosted CDI capability, Sep. Purif. Technol. 345 (2024) 127380, https://doi.org/10.1016/j.seppur.2024.127380.

[51] Y. Li, Y. Cai, Y. Wang, D. Liu, J. Guo, A Study of 3D flake MnO_2 nanoflower decorated hollow carbon spheres as cathode material for pseudo-capacitive deionization, J. Environ. Chem. Eng. 10 (2) (2022) 107266, https://doi.org/10.1016/j.jece.2022.107266.

[52] Y. Lei, S. Wang, L. Zhao, C. Li, G. Wang, J. Qiu, Entropy engineering constrain phase transitions enable ultralong-life prussian blue analogs cathodes, 2402340, Adv. Sci. (Weinh) (2024), https://doi.org/10.1002/advs.202402340.